

Antimonene: A Novel 2D Nanomaterial for Supercapacitor Applications

Emiliano Martínez-Periñán, Michael P. Down, Carlos Gibaja, Encarnación Lorenzo, Félix Zamora,* and Craig E. Banks*

In pursuing higher energy density, without compromising the power density of supercapacitor platforms, the application of an advanced 2D nanomaterial is utilized to maximize performance. Antimonene, for the first time, is characterized as a material for applications in energy storage, being applied as an electrode material as the basis of a supercapacitor. Antimonene is shown to significantly improve the energy storage capabilities of a carbon electrode in both cyclic voltammetry and galvanostatic charging. Antimonene demonstrates remarkable performance with a capacitance of 1578 F g^{-1} , with a high charging current density of 14 A g^{-1} . Hence, antimonene is shown to be a highly promising material for energy storage applications. The system also demonstrates a highly competitive energy and power densities of 20 mW h kg^{-1} and 4.8 kW kg^{-1} , respectively. In addition to the excellent charge storing abilities, antimonene shows good cycling capabilities.

and hybrid electric vehicles to mobile phones.^[2]

Advances in nanomaterials and nanotechnology are playing a key role in bringing EDLC toward practical applications and improvement in device performance, scale, and compatibility. In particular, more attention has been paid to the development of new nanomaterials, which are expected to allow the development of electrodes with major storage capability.^[3] Indeed, 2D nanomaterials have spiked interest due to their high specific surface area, a material property that can significantly contribute to a high double-layer capacitance. Furthermore, 2D nanomaterials have reactive basal planes and edges that can provide electrochem-

ical performance enhancement such as pseudocapacitance.^[4] After graphene's successful application in different energy storage devices,^[5] new 2D inorganic nanomaterials have been developed,^[6] most with related layered crystalline structures.^[7] Such 2D nanomaterials have shown great promise as electrode materials when layered onto the electrodes in electrochemical energy-storage devices in which efficient intercalation of ions plays an important role.^[8] They involve van der Waals interactions between adjacent sheets, with strong covalent bonding within each sheet. There are important reasons for the exploration of these nanomaterials. In particular, that mono- or few-layer materials show increased bandgap and tunable electronic, optical, catalytic, and electrochemical properties.^[9] Thus, some of these materials span the entire range of electronic structures,

1. Introduction

The increasing demand and development of renewable and sustainable energy sources have required sustainable energy storage technologies, in order to satisfy the demand for green energy.^[1] Because of their high power density, good operational safety, long cycling life, competitive energy density, and minimum charge separation compared to alternative energy storage platforms, electrochemical double-layer capacitors (EDLC) or supercapacitors have been considered as an energy storage platform with significant potential. Supercapacitors have been extensively explored and are recognized as promising devices for energy applications from high-power electronics down to fast charging personal electronic devices, from electric vehicles

Dr. E. Martínez-Periñán, Prof. E. Lorenzo
Departamento de Química Analítica y Análisis Instrumental
Institute for Advanced Research in Chemical Sciences (IAdChem)
Universidad Autónoma de Madrid
28049 Madrid, Spain


Dr. E. Martínez-Periñán, Dr. M. P. Down, Prof. C. E. Banks
Faculty of Science and Engineering
Manchester Metropolitan University
Chester Street, Manchester M1 5GD, UK

Dr. M. P. Down, Prof. C. E. Banks
Manchester Fuel Cell Innovation Centre
Manchester Metropolitan University
Chester Street, Manchester M1 5GD, UK
E-mail: c.banks@mmu.ac.uk

C. Gibaja, Prof. F. Zamora
Departamento de Química Inorgánica and Institute for Advanced
Research in Chemical Sciences (IAdChem)
Universidad Autónoma de Madrid
28049 Madrid, Spain
E-mail: felix.zamora@uam.es

Prof. E. Lorenzo, Prof. F. Zamora
Instituto Madrileño de Estudios Avanzados en Nanociencia
(IMDEA-Nanociencia)
Cantoblanco, Madrid E-28049, Spain

Prof. F. Zamora
Condensed Matter Physics Center (IFIMAC)
Universidad Autónoma de Madrid
Madrid E-28049, Spain

 The ORCID identification number(s) for the author(s) of this article can be found under <https://doi.org/10.1002/aenm.201702606>.

DOI: 10.1002/aenm.201702606

from insulator to metal, and display intriguing properties.^[10] Recently, some studies have been successfully being carried out on the electrochemical applications of graphene-like layered materials such as transition metal dichalcogenides.^[11] Additionally, some of the new 2D nanomaterials such as 2D h-boron nitride,^[12] metal oxides,^[13] metal carbides,^[14] and metal dichalcogenides^[15] are showing desirable performance in supercapacitor applications.

In recent years, a new family of compounds similar to graphene, based on anisotropic layered elemental materials, are attracting the attention of the scientific community. These materials, ideally, consist of one atom thick type 2D structure; each atom is covalently bonded with adjacent atoms to form a puckered honeycomb structure. For example, phosphorene, from an allotrope of phosphorous, black-phosphorus,^[16] is worthwhile to be mentioned because of the interesting properties with applications in optoelectronics and electronics^[17] and in energy storage devices.^[18] The success of phosphorene has carried on the attention to the rest of fifth main group of elements,^[9] and new materials such as arsenene, antimonene, and bismuthene have been predicted with interesting properties,^[19] and even so some of them have been isolated.^[20] Antimonene is considered a material of great interest for applications in electrochemistry and has been also isolated from its layered allotrope form. First, it has been isolated by mechanical exfoliation^[21] and then by liquid-phase exfoliation.^[22] Importantly, in these works, antimonene was proved to have high environmental stability.^[23]

Recent theoretical and experimental studies have highlighted antimonene's attractive properties including its puckered lamellar structure (which significantly increases its specific surface area), good electrical conductivity ($1.6 \times 10^4 \text{ S m}^{-1}$),^[23b] thermodynamic stability, large interlayer channel size (3.73 \AA),^[21] and fast ion diffusion properties,^[24] making it an ideal candidate for electrochemical storage energy applications. Recent work has also demonstrated its potential, and attractive application as an anode material in lithium and sodium ion batteries^[25] due to its ability to enable fast ionic diffusion over its surface.^[24] However, although antimonene is also a great candidate for supercapacitor development, again because it exhibits fast interlayer ionic transport,^[24,26] it has never been used for this application.

Using those observations as a point of departure, in this work, we have focused on the electrochemical capacitive performance of antimonene flakes. While there are only a limited number of electrochemical studies on this new 2D nanomaterial, we have demonstrated its successful application as a supercapacitor, obtaining high specific capacitance values, demonstrating its promise for use in electrical energy storage applications.

2. Results and Discussion

2.1. Antimonene Material Characterization

Few-layer (FL)-antimonene has been prepared following a modification of the liquid-phase exfoliation (LPE) procedure already reported in the literature.^[22] The new preparation involves a first step in which antimony crystals were treated within a ball-mill

for 180 min at 3000 rpm. This first step produces an evident size reduction of the antimony crystals as well as a more homogeneous material in size. Scanning electron microscopy (SEM) images of the antimony powder obtained after ball-milling step confirm the formation of microcrystals with dimensions in the range of $1 \text{ }\mu\text{m}$, which is significantly smaller and more homogeneous than the commercial crystals (Figure S1, Supporting Information). The resulting microcrystalline powder was then suspended in a mixture 4:1 isopropanol ($i\text{PrOH}$)-water and sonicated for 40 min to produce a very stable suspension, over weeks, of FL-antimonene even in ambient conditions (Figure S2, Supporting Information). The so-formed suspension shows Faraday-Tyndall effect (Figure S2, Supporting Information). The unexfoliated material was removed by centrifugation at 845 rcf for 3 min to produce a stable dispersion with a concentration of $\approx 0.014 \text{ g L}^{-1}$, which is significantly much higher to that previously reported by us.^[22] The significant enhancement in the concentration of the antimonene suspension is critical to get a suitable electrode deposition. It is remarkable that previous attempts to use antimonene suspensions as smaller as those obtained in ref. [22] $\approx 1.74 \times 10^{-3} \text{ g L}^{-1}$, experimentally failed. It seems that the concentration of antimonene reach these higher values, in comparison to those previously reported, due to the initial ball-milling step since this treatment provides a more homogeneous starting material with smaller lateral dimensions. The exfoliation of the antimony microcrystals upon sonication was confirmed by atomic force microscopy (AFM). Figure S3 (Supporting Information) shows a characteristic topographic image of FL-antimonene flakes isolated on SiO_2 substrates. Interestingly, the flakes do not show typical terraces characteristic of layered materials but well-defined structures with heights being multiple of $\approx 4 \text{ nm}$. Similar observations were already done in the reported antimony LPE procedures.^[22] These results suggest that the two-step procedure leads to the formation of few-layer-antimonene since it is well-known that apparent AFM heights of layers obtained by LPE can be overestimated due to residual solvent,^[27] therefore it seems likely that the apparent mono-/bilayer thickness could correspond to $\approx 4\text{--}5 \text{ nm}$. We note that the overall lateral dimensions of the isolated nanosheets are in the range of $1\text{--}3 \text{ }\mu\text{m}^2$. High-resolution transmission electron microscopy (HRTEM) measurements further confirm the exfoliation and the crystallinity of the FL-antimonene (Figure 1). Energy-dispersive X-ray (EDX) spectra confirm the layer composition, which consists almost exclusively on antimony with a very low content of oxygen (Figure S4, Supporting Information).

2.2. Antimonene Modified Screen-Printed Electrode (SPE) Characterization

Antimonene modified SPEs have been characterized by SEM and Raman spectroscopy in order to confirm the proper modification of the electrodes with the 2D nanomaterial. SEM images (Figure 2A–C) clearly show the deposit of small flakes of antimonene compared with the bare SPE SEM image (Figure 2D). As can be observed in SEM images, shown in Figure 2, antimonene forms flakes with lateral dimension around $200\text{--}400 \text{ nm}$. This is a typical antimonene morphology,

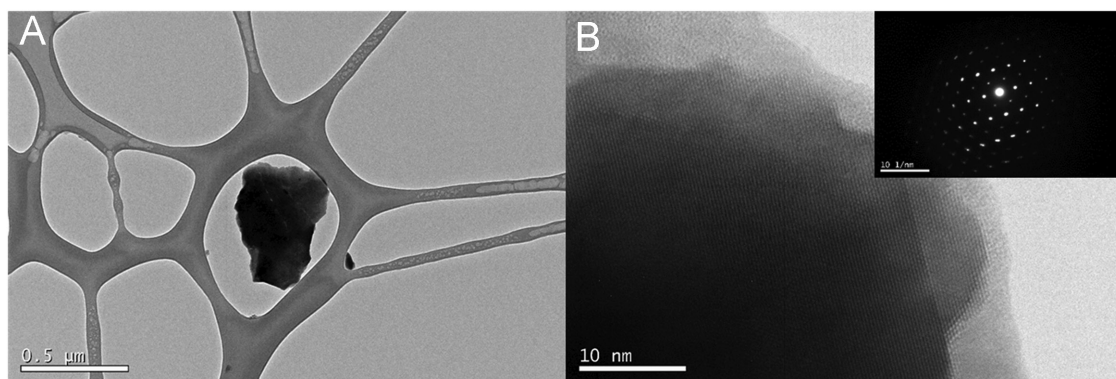


Figure 1. A) TEM image of a thin antimony flake. B) Magnification of same flake showing atomic resolution. The inset shows electron diffraction pattern, displaying the expected hexagonal symmetry for β -antimony.

agreeing well with that described in the literature describing the synthesis.^[22] The atomic composition of the flakes is antimony, Sb, as can be determined by EDX spectrum (Figure S5 and Table S1, Supporting Information).

Raman spectroscopy also confirms the presence of antimonene over the modified SPE surface (Figure 3A,B). In addition to the Raman bands associated with carbon, which constitutes the base of the SPE, two Raman bands, associated with the antimony (Sb) A_{1g} and E_g vibrational modes at 150 cm^{-1} and mode at 110 cm^{-1} , respectively, were detected. The intensity of these bands increases when higher amounts of antimonene are drop-casted over the SPE surface, which indicates at the same time higher antimony deposition and even that the thickness of these nanostructures could increase. This

fact could be related with the decrease of capacitance observed in the next showed results, when higher amounts of antimonene are drop-casted over the SPE, being consequence of less electroactive surface of the 2D nanomaterial when higher nanostructures are deposited or the stack of the small few-layer-antimonene flakes occurs.

2.3. Exploring Antimonene as a Capacitive Material

We first consider the cyclic voltammetric responses of the bare SPE utilizing a two-electrode system in $0.5\text{ M H}_2\text{SO}_4$ at different scan rates, which provide a benchmark, after which we analyzed the response exhibited upon drop-casting of antimonene,

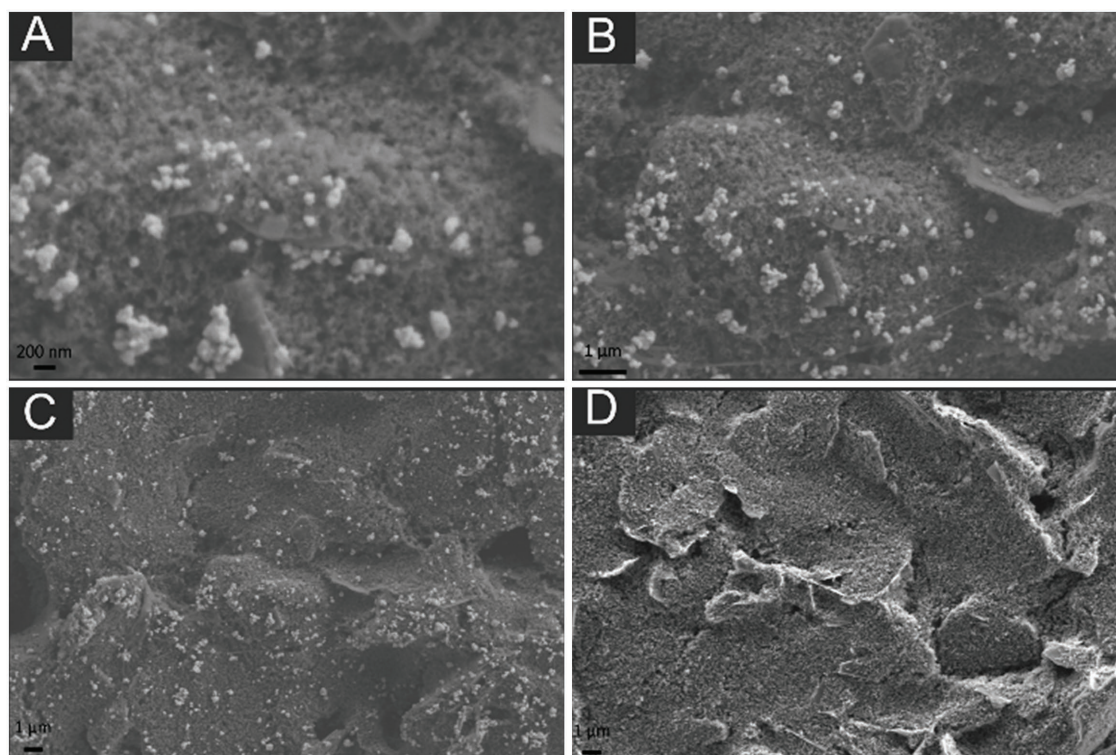


Figure 2. SEM images at different magnifications of A–C) 36 ng antimonene/SPE and D) bare SPE.

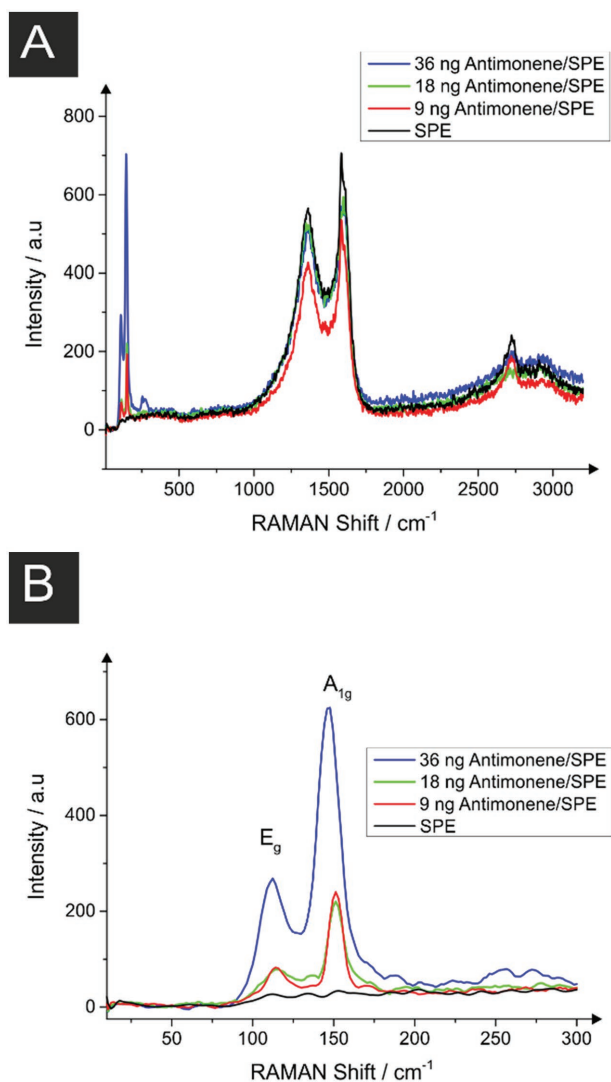


Figure 3. A,B) Raman spectra of bare SPE and modified antimonene/SPE with different amounts of antimonene.

amounts ranging from 1.8 to 36 ng (Figure 4A–C). The increase of capacitive current when small amounts of antimonene are drop-casted onto the SPE can be clearly observed. Even so, a redox process is observed at formal potential 0.0 V, which could be ascribed to the oxidation and reduction of antimonene, as a consequence of a Faradaic process, which also contributes significantly to the capacitance increase.

The capacitance of the working electrode, C_{we} , was calculated from the corresponding voltammograms, as shown in Figure 4, using the following Equation (1)

$$C_{we} = \frac{\int_{V_1}^{V_2} I(V) dV}{2 \times \Delta V \times \nu \times m} \quad (1)$$

where C_{we} is the specific capacitance exhibited by the working electrode in Faradays per gram ($F g^{-1}$), $\int I(V) dV$ is the area under the intensity current function between V_2 and V_1 poten-

tials in Coulombs (C), essentially a measure of the charge stored by the capacitor device. ΔV is the potential difference between V_2 and V_1 in volts (V), ν is the voltammogram scan rate in volts per second ($V s^{-1}$), and m is the material (antimonene) mass in grams. The determined capacitance values are shown in Table S2 (Supporting Information). Exceptional capacitance values are obtained, being around $8500 F g^{-1}$. This large value determined is the consequence of the combination of two factors, the increase of electrochemical active area and the consequent increase of the electrochemical double layer over the electrode surface. On the other hand, these large values are a consequence of the Faradaic process described, increasing the area under the current curves because of the redox peak.

In order to have more realistic capacitance values, galvanostatic charge/discharge study was performed using a two-electrode approach to compliment the setup utilized for supercapacitors within the field. Figure 5A illustrates the charge/discharge profiles obtained for bare SPE, and antimonene modified SPE with increasing amounts of the 2D nanomaterial. The results clearly show that dV/dt decreases, which is a consequence of the capacitance increase when SPE is modified with the 2D nanomaterial. Capacitance values and specific capacitance values are shown in Table 1 and Table S3 (Supporting Information), respectively. These values are lower than the obtained by cyclic voltammetry (CV), but we consider it more realistic values, and no Faradaic process is involved in that case. The specific capacitance in the best configuration 3.6 ng antimonene/SPE at a current of $14 A g^{-1}$ is $1578 F g^{-1}$ (Figure 5C). This high value is competitive with other 2D nanomaterials that are being proving as supercapacitor material,^[12,28] and with other types of material used in supercapacitors.^[29] As can be seen (Figure 5B), the absolute capacitance values increase with the amount of antimonene deposited onto the SPE surface until we modified it with 18.0 ng antimonene. From that 2D nanomaterial mass, the capacitance decreases, which could be a consequence of the nanomaterial agglomeration or stacking, decreasing the electroactive surface area.

For supercapacitors, cycling stability is also a very important parameter. Therefore, the charge–discharge stability was studied over 10 000 galvanostatic cycles, applying a specific current of $14 A g^{-1}$ on a 36 ng antimonene/SPE (Figure 5D). The capacitance retention values demonstrate that after an initial drop to 65%, the successive cycles retain the capacitance between 65% and 63% of the initial capacitance over the entire range of cycles, showing the same capacitance between the scan 800 and the 10 000. This result proved that after an initial stabilization, the capacitance keeps constant at least more than 9000 charge–discharge cycles, the maximum number of cycles that has been experimentally studied on this work. It is likely that the decrease in the first 1000 cycles can be attributed to some of the drop-cast antimonene being liberated from the electrode surface with charge cycling.

Typically, a supercapacitor exhibits a low energy density, E , and a high power density, P , the values of which are calculated using $E = \int I(dV)(dt)/2m$ and $P = (I(dV))/2m$, respectively, where m is the mass of the antimonene residing upon the surface of the SPE (i.e., 1.8 ng), in this case the values correspond to

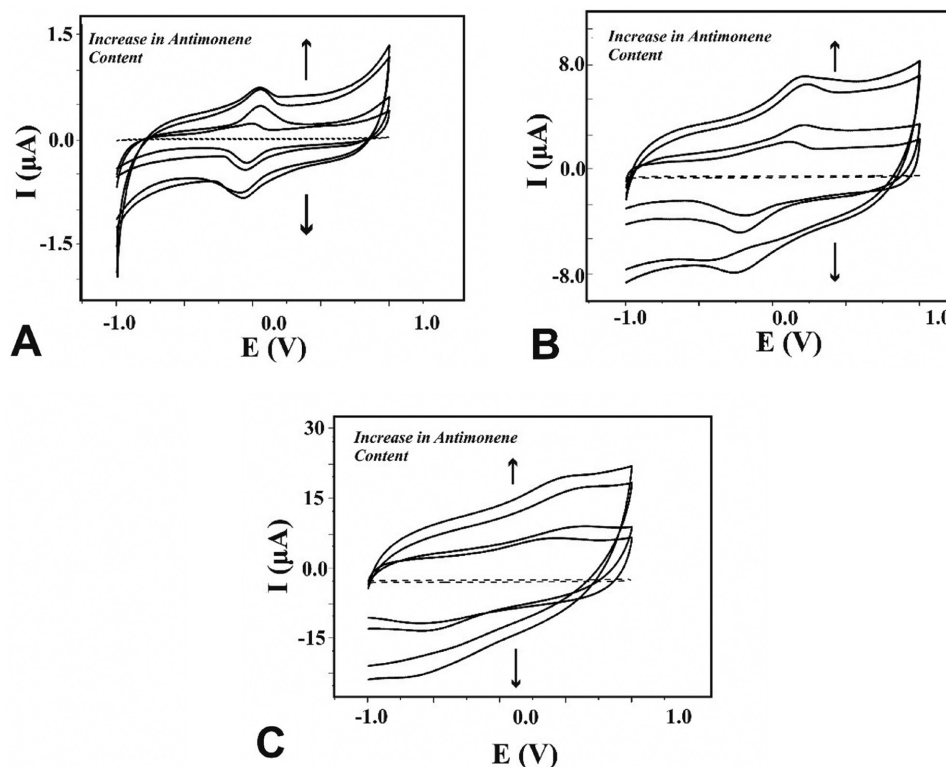


Figure 4. Cyclic voltammograms obtained with a two electrodes system of SPE and different amounts of antimonene modified SPE at A) 10 mV s^{-1} , B) 100 mV s^{-1} , and C) 500 mV s^{-1} in 0.5 M H_2SO_4 . It becomes clear that the integral area of the CVs, a property that is indicative of the capacitance of the system, is directly proportional to the quantity of antimonene present on the electrode.

0.02 W h kg^{-1} and 4800 W kg^{-1} , respectively. These values are indicative of a high power supercapacitor (Figure 6).

3. Conclusion

Antimonene, for the first time, is characterized as a material for applications in energy storage, being applied as an electrode material for supercapacitors. It is shown to significantly improve the energy storage capabilities of a carbon electrode substrate in both cyclic voltammetry and galvanostatic charging, demonstrating remarkable performance with a capacitance of 1578 F g^{-1} with a high charging current density of 14 A g^{-1} . Antimonene is shown to be a promising material for energy storage applications. The antimonene enhanced electrodes demonstrate a pseudocapacitive Faradaic voltammetric response, which is shown to enhance the electrochemical capacitive performance of the electrode materials. The presence of the antimonene is shown to significantly increase the capacitive performance of the supercapacitors when compared to a device with bare graphitic electrodes. Quantities of antimonene as little as 1.8 ng of material are shown to significantly improve the capacitive performance of the system. The system also demonstrates a highly competitive energy and power densities of 20 mW h kg^{-1} and 4.8 kW kg^{-1} , respectively. As well as due to excellent charge storing capabilities, the antimonene demonstrates good cycling capabilities

over 1000 cycles until the drop-cast material is liberated from the substrate.

4. Experimental Section

All chemicals utilized were of analytical grade and were used as received from Sigma-Aldrich without any further purification. Commercially available antimony material (99.9999% Smart Elements), and 2-propanol (99.8% Panreac) were used without further purification. All solutions were prepared with deionized water of resistivity not less than 18.2 $\text{M}\Omega \text{ cm}$ and (when necessary) were vigorously degassed prior to electrochemical measurements with high purity, oxygen free nitrogen.

Standard Liquid Phase Exfoliation Procedure: 100 mg of powdered antimony was submitted to a 20 mL ball-milled reactor charged with 30 stainless steel balls (0.5 cm diameter), to complete a total volume of ≈ 7.5 mL. The mixture was treated 180 min at 3000 rpm. 10 mg of the resulting powder was mixed with 10 mL of a 4:1 2-propanol: water mixture in a 20 mL vial and sonicated for 40 min at 400 W and 24 kHz, delivering the ultrasound power in pulses 0.5 s long every 1 s. The resulting suspension was centrifuged at 3000 rpm (845 rcf) for 3 min and the clear supernatant collected as final suspension. The concentration of the suspension was evaluated using atomic absorption spectrometry and its stability with the time using turbidimetry measurements.

Sonication was performed using a Hielscher UP400S ultrasonic processor equipped with a 3 mm sonotrode.

Methods: The milling process was carried out using an IKA ULTRA-TURRAX Tube Drive control equipped with the BMT-20 reactor and stainless steel balls.

Centrifugation was carried out in a MPW-350R centrifuge using 2 mL Eppendorfs.

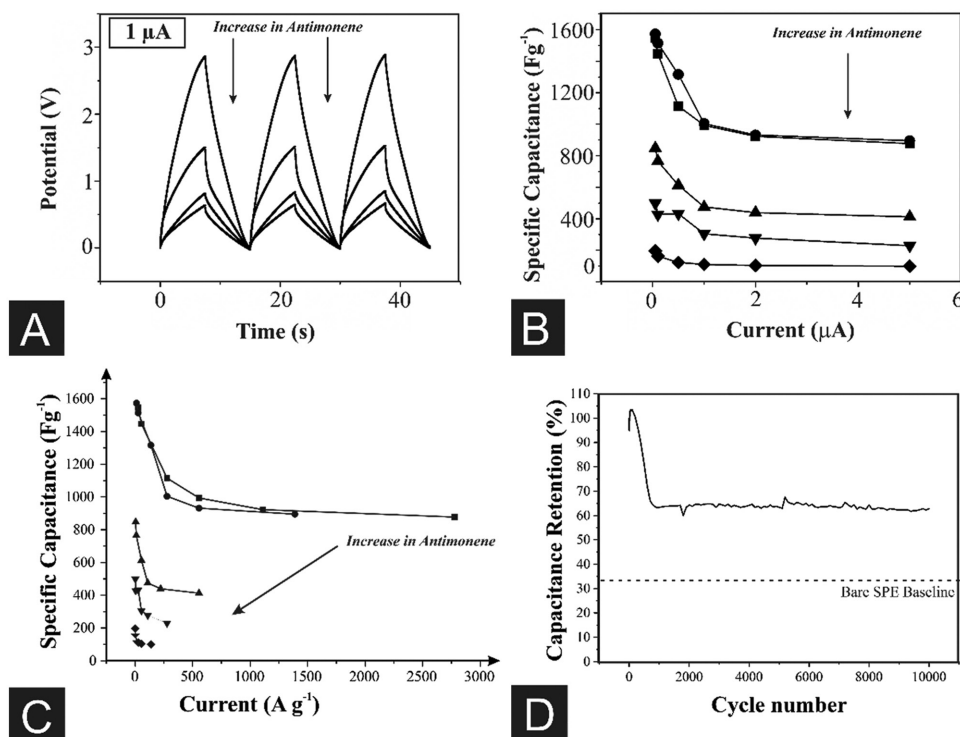


Figure 5. A) Charge/discharge profiles recorded in 0.5 M H_2SO_4 with unmodified and antimonene modified SPEs (increasing the antimonene amount from 1.8 to 36.0 ng) applying 1.00 μA . B) Capacitance values versus current applied obtained from charge–discharge profiles. C) Specific capacitance values versus specific current applied obtained from charge–discharge profiles. D) Relative capacitance for successive charge–discharge cycles respect the first cycle capacitance. The capacitance of the bare SPE, on its first cycle, is also indicated. It is shown that the antimonene enhanced electrodes are consistently performing higher than the bare SPE.

Sonication was performed using a Hielscher UP400S ultrasonic processor equipped with a 3 mm sonotrode.

Antimony determination was carried out by flame atomic absorption spectrometry using a ContraAA 700 high-resolution atomic absorption spectrometer (Analytik Jena, Germany). The main line for antimony at 217.5815 nm was employed for all the analysis. The atomization was performed using an air acetylene flame with an acetylene flow rate of 60 L h^{-1} and at a 6.0 mm burner height. The aspiration rate was fixed at 5 mL min^{-1} . All measurements were carried out in triplicate.

Measurements were carried out using a HI-88713 Bench Top Turbidity Meter Hanna Instruments.

AFM measurements were carried out using a Cervantes Fullmode AFM from Nanotec Electronica SL. WSxM software (www.wsxmsolutions.com) was employed both for data acquisition and image processing.^[30] All the topographical images shown in this work were acquired in contact

Table 1. Capacitance values obtained from charge–discharge profiles for different amounts of antimonene modified SPEs at different currents in microfarad.

Current [μA]	Antimonene mass [ng]				
	1.8	3.6	9.0	18.0	36.0
0.05	2.78	5.66	7.63	8.98	7.05
0.10	2.60	5.45	6.89	7.69	5.88
0.50	2.01	4.74	5.52	7.79	4.43
1.00	1.79	3.62	4.27	5.47	3.99
2.00	1.66	3.36	3.95	4.99	3.74
5.00	1.58	3.22	3.71	4.12	3.58

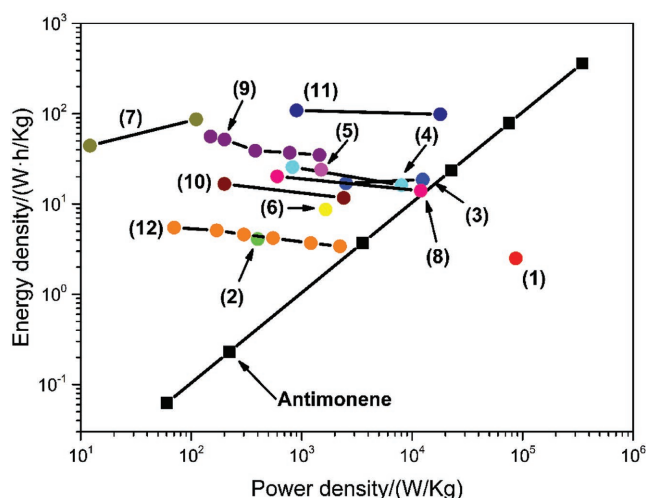


Figure 6. Ragone plot showing the results obtained for antimonene/SPE and some actual data obtained at bibliography of 2D nanomaterial or modified 2D nanomaterials.^[28b,c,31] The antimonene supercapacitor, shown as black squares, is compared to: (1) a graphene/sodium cholate enhanced electrode;^[31b] (2) reduced graphene oxide paper electrodes;^[31a] (3) 2D nanosheets d- MnO_2 /graphene electrodes;^[31d] (4) reduced graphene oxide- MnO_2 nanocomposite;^[31d] (5) nitrogen crumpled graphene sheets;^[31e] (6) 3D nitrogen and boron codoped graphene;^[31a] (7) nitrogen enriched carbon nanosheets;^[31f] (8) RuO_2 /graphene hybrid material;^[31g] (9) $\text{Ni}(\text{OH})_2$ /reduced graphene oxide composites;^[28c] (10) NiCo_2S_4 nanosheets;^[31h] (11) single layer b- $\text{Co}(\text{OH})_2$;^[28b] and (12) 2D Ti_3C_2 2D nanosheets.^[31i]

mode to avoid possible artifacts in the flake thickness measurements.^[32] OMCL-RC800PSA cantilevers (probe.olympus-global.com) with a nominal spring constant of 0.39 N m⁻¹ and tip radius of 15 nm were employed. Low forces of the order of 1 nN were used for imaging to ensure that the flakes would not be deformed by the tip.

SiO₂ surfaces were sonicated for 15 min in acetone and 15 min in 2-propanol and then dried under an argon flow.

TEM images were obtained in a JEOL JEM 2100 FX TEM system with an accelerating voltage of 200 kV. The microscope has a multiscan charge-coupled device camera ORIUS SC1000 and an OXFORD INCA X-Ray Energy Dispersive Spectroscopy microanalysis system.

Scanning transmission electron microscopy combined with electron energy-loss spectroscopy (EELS) was used at 80 kV in a JEOL ARM200cF equipped with a spherical aberration corrector and a Gatan Quantum EEL spectrometer.

The working electrodes used were SPEs. The SPEs, which have a 3 mm diameter working electrode, were fabricated in-house with appropriate stencil designs using a microDEK 1760RS screen-printing machine (DEK, Weymouth, UK). The SPE design was previously reported.^[33] For the case of each fabricated electrode, first a graphite ink formulation (Product Code: C2000802P2; Gwent Electronic Materials Ltd, UK), which was utilized for the efficient connection of all three electrodes and as the ink material for both the working and counter electrodes, was screen-printed onto a polyester (Autostat, 250 mm thickness) Flexible film. After curing the screen-printed graphite layer in a fan oven at 60 °C for 30 min. Finally, a dielectric paste (Product Code: D2070423D5; Gwent Electronic Materials Ltd, UK) was then screen-printed onto the polyester substrate to cover the connections and define the active electrode areas, including that of the working electrode (3 mm diameter). After curing at 60 °C for 30 min, the SPEs were ready to be used.

Antimonene modified electrodes were prepared by drop-casting aliquots of the 0.02 g L⁻¹ antimonene 4:1 isopropanol/water suspension onto the required working electrode with a micropipette. After a few minutes, the solvent completely evaporated (at ambient temperature) and the modified electrodes were utilized without further modification. All electrochemical measurements were performed with an Autolab TYPE III (Autolab, The Netherlands). It was noted that the charge-discharge curves and cyclic voltammetry for capacitance measures were obtained using a two-electrode configuration.

SEM images and surface element analysis of antimonene/SPE were carried on using a JEOL JSM-5600LV model equipped with an EDX microanalysis package.

Raman spectroscopy analysis of antimonene modified SPE surfaces was done using a "Renishaw InVia" spectrometer with a confocal microscope (50× objective) spectrometer with an argon laser (514.3 nm excitation) at a very low laser power level (1.2 mW) to avoid any heating effects. Spectra were obtained using a 10 s exposure time for three accumulations.

Supporting Information

Supporting Information is available from the Wiley Online Library or from the author.

Acknowledgements

Funding from the Engineering and Physical Sciences Research Council (Reference: EP/N001877/1), the British Council Institutional Grant Link (No. 172726574), and the Spanish MICINN (grant MAT2016-77608-C3-1-P) is acknowledged. E.M.-P. acknowledges funding from the Comunidad de Madrid (NANOAVANSENS Program) for financial support.

Conflict of Interest

The authors declare no conflict of interest.

Keywords

2D nanomaterials, antimonene, EDLC, liquid-phase exfoliation, supercapacitors

Received: September 18, 2017

Revised: October 10, 2017

Published online:

- [1] a) H. D. Abruña, J. Chem. Educ. **2013**, 90, 1411; b) J. Chow, R. J. Kopp, P. R. Portney, Science **2003**, 302, 1528.
- [2] a) R. Kötz, M. Carlen, Electrochim. Acta **2000**, 45, 2483; b) A. González, E. Goikolea, J. A. Barrena, R. Mysyk, Renewable Sustainable Energy Rev. **2016**, 58, 1189; c) L. L. Zhang, X. S. Zhao, Chem. Soc. Rev. **2009**, 38, 2520.
- [3] P. Thangavelu, B. Jong-Beom, 2D Mater. **2015**, 2, 032002.
- [4] B. Mendoza-Sánchez, Y. Gogotsi, Adv. Mater. **2016**, 28, 6104.
- [5] a) P. Xiong, J. Zhu, L. Zhang, X. Wang, Nanoscale Horiz. **2016**, 1, 340; b) M. F. El-Kady, Y. Shao, R. B. Kaner, Nat. Rev. Mater. **2016**, 1, 16033; c) L. Wen, F. Li, H.-M. Cheng, Adv. Mater. **2016**, 28, 4306; d) J. Ji, Y. Li, W. Peng, G. Zhang, F. Zhang, X. Fan, Adv. Mater. **2015**, 27, 5264.
- [6] C. Tan, X. Cao, X.-J. Wu, Q. He, J. Yang, X. Zhang, J. Chen, W. Zhao, S. Han, G.-H. Nam, M. Sindoro, H. Zhang, Chem. Rev. **2017**, 117, 6625.
- [7] Q. Tang, Z. Zhou, Z. Chen, Wiley Interdiscip. Rev.: Comput. Mol. Sci. **2015**, 5, 360.
- [8] a) E. Yoo, J. Kim, E. Hosono, H.-S. Zhou, T. Kudo, I. Honma, Nano Lett. **2008**, 8, 2277; b) L. Mai, H. Li, Y. Zhao, L. Xu, X. Xu, Y. Luo, Z. Zhang, W. Ke, C. Niu, Q. Zhang, Sci. Rep. **2013**, 3, 1718.
- [9] M. Pumera, Z. Sofer, Adv. Mater. **2017**, 29, 1605299.
- [10] M. Xu, T. Liang, M. Shi, H. Chen, Chem. Rev. **2013**, 113, 3766.
- [11] S. J. Rowley-Neale, J. M. Fearn, D. A. C. Brownson, G. C. Smith, X. Ji, C. E. Banks, Nanoscale **2016**, 8, 14767.
- [12] A. F. Khan, M. P. Down, G. C. Smith, C. W. Foster, C. E. Banks, J. Mater. Chem. A **2017**, 5, 4103.
- [13] a) W. Sugimoto, H. Iwata, Y. Yasunaga, Y. Murakami, Y. Takasu, Angew. Chem., Int. Ed. **2003**, 42, 4092; b) K. Kai, Y. Kobayashi, Y. Yamada, K. Miyazaki, T. Abe, Y. Uchimoto, H. Kageyama, J. Mater. Chem. **2012**, 22, 14691; c) X. Xiao, H. Song, S. Lin, Y. Zhou, X. Zhan, Z. Hu, Q. Zhang, J. Sun, B. Yang, T. Li, L. Jiao, J. Zhou, J. Tang, Y. Gogotsi, Nat. Commun. **2016**, 7, 11296.
- [14] J. Li, X. Yuan, C. Lin, Y. Yang, L. Xu, X. Du, J. Xie, J. Lin, J. Sun, Adv. Energy Mater. **2017**, 7, 1602725.
- [15] M. Acerce, D. Voiry, M. Chhowalla, Nat. Nanotechnol. **2015**, 10, 313.
- [16] L. Wang, Z. Sofer, M. Pumera, ChemElectroChem **2015**, 2, 324.
- [17] a) L. Li, Y. Yu, G. J. Ye, Q. Ge, X. Ou, H. Wu, D. Feng, X. H. Chen, Y. Zhang, Nat. Nanotechnol. **2014**, 9, 372; b) M. Buscema, D. J. Groenendijk, S. I. Blanter, G. A. Steele, H. S. J. van der Zant, A. Castellanos-Gomez, Nano Lett. **2014**, 14, 3347.
- [18] a) C. Hao, B. Yang, F. Wen, J. Xiang, L. Li, W. Wang, Z. Zeng, B. Xu, Z. Zhao, Z. Liu, Y. Tian, Adv. Mater. **2016**, 28, 3194; b) C. M. Park, H. J. Sohn, Adv. Mater. **2007**, 19, 2465; c) J. Sun, G. Zheng, H.-W. Lee, N. Liu, H. Wang, H. Yao, W. Yang, Y. Cui, Nano Lett. **2014**, 14, 4573; d) J. Song, Z. Yu, M. L. Gordin, S. Hu, R. Yi, D. Tang, T. Walter, M. Regula, D. Choi, X. Li, A. Manivannan, D. Wang, Nano Lett. **2014**, 14, 6329.
- [19] a) S. Zhang, M. Xie, F. Li, Z. Yan, Y. Li, E. Kan, W. Liu, Z. Chen, H. Zeng, Angew. Chem., Int. Ed. **2016**, 55, 1666; b) C. Kamal, M. Ezawa, Phys. Rev. B **2015**, 91, 085423; c) Z. Zhu, J. Guan, D. Tománek, Phys. Rev. B **2015**, 91, 161404.
- [20] a) E. S. Walker, S. R. Na, D. Jung, S. D. March, J.-S. Kim, T. Trivedi, W. Li, L. Tao, M. L. Lee, K. M. Liechti, D. Akinwande, S. R. Bank,

- Nano Lett.* **2016**, *16*, 6931; b) X. Wu, Y. Shao, H. Liu, Z. Feng, Y.-L. Wang, J.-T. Sun, C. Liu, J.-O. Wang, Z.-L. Liu, S.-Y. Zhu, Y.-Q. Wang, S.-X. Du, Y.-G. Shi, K. Ibrahim, H.-J. Gao, *Adv. Mater.* **2017**, *29*, 1605407.
- [21] P. Ares, F. Aguilar-Galindo, D. Rodríguez-San-Miguel, D. A. Aldave, S. Díaz-Tendero, M. Alcamí, F. Martín, J. Gómez-Herrero, F. Zamora, *Adv. Mater.* **2016**, *28*, 6332.
- [22] C. Gibaja, D. Rodríguez-San-Miguel, P. Ares, J. Gómez-Herrero, M. Varela, R. Gillen, J. Maultzsch, F. Hauke, A. Hirsch, G. Abellán, F. Zamora, *Angew. Chem., Int. Ed.* **2016**, *55*, 14345.
- [23] a) S. Zhang, Z. Yan, Y. Li, Z. Chen, H. Zeng, *Angew. Chem., Int. Ed.* **2015**, *54*, 3112; b) J. Ji, X. Song, J. Liu, Z. Yan, C. Huo, S. Zhang, M. Su, L. Liao, W. Wang, Z. Ni, Y. Hao, H. Zeng, *Nat. Commun.* **2016**, *7*, 13352; c) S. Zhang, W. Zhou, Y. Ma, J. Ji, B. Cai, S. A. Yang, Z. Zhu, Z. Chen, H. Zeng, *Nano Lett.* **2017**, *17*, 3434.
- [24] A. Sengupta, T. Frauenheim, *Mater. Today Energy* **2017**, *5*, 347.
- [25] a) M. He, K. Kravchyk, M. Walter, M. V. Kovalenko, *Nano Lett.* **2014**, *14*, 1255; b) M. Walter, R. Erni, M. V. Kovalenko, *Sci. Rep.* **2015**, *5*, 8418.
- [26] X. Ren, P. Lian, D. Xie, Y. Yang, Y. Mei, X. Huang, Z. Wang, X. Yin, *J. Mater. Sci.* **2017**, *52*, 10364.
- [27] a) K. R. Paton, E. Varrla, C. Backes, R. J. Smith, U. Khan, A. O'Neill, C. Boland, M. Lotya, O. M. Istrate, P. King, T. Higgins, S. Barwich, P. May, P. Puczkarski, I. Ahmed, M. Moebius, H. Pettersson, E. Long, J. Coelho, S. E. O'Brien, E. K. McGuire, B. M. Sanchez, G. S. Duesberg, N. McEvoy, T. J. Pennycook, C. Downing, A. Crossley, V. Nicolosi, J. N. Coleman, *Nat. Mater.* **2014**, *13*, 624; b) D. Hanlon, C. Backes, E. Doherty, C. S. Cucinotta, N. C. Berner, C. Boland, K. Lee, A. Harvey, P. Lynch, Z. Gholamvand, S. F. Zhang, K. P. Wang, G. Moynihan, A. Pokle, Q. M. Ramasse, N. McEvoy, W. J. Blau, J. Wang, G. Abellán, F. Hauke, A. Hirsch, S. Sanvito, D. D. O'Regan, G. S. Duesberg, V. Nicolosi, J. N. Coleman, *Nat. Commun.* **2015**, *6*, 8563.
- [28] a) H. Chen, H. Gao, H. Xiao, X. Zhou, W. Zhang, Q. Ling, *Electrochim. Acta* **2016**, *206*, 10; b) S. Gao, Y. Sun, F. Lei, L. Liang, J. Liu, W. Bi, B. Pan, Y. Xie, *Angew. Chem., Int. Ed.* **2014**, *53*, 12789; c) Z. Li, W. Zhang, C. Sun, Z. Feng, B. Yang, *Electrochim. Acta* **2016**, *212*, 390.
- [29] a) Y. Li, X. Wang, Q. Yang, M. S. Javed, Q. Liu, W. Xu, C. Hu, D. Wei, *Electrochim. Acta* **2017**, *234*, 63; b) X. Wang, B. Shi, Y. Fang, F. Rong, F. Huang, R. Que, M. Shao, *J. Mater. Chem. A* **2017**, *5*, 7165; c) M. E. Roberts, D. R. Wheeler, B. B. McKenzie, B. C. Bunker, *J. Mater. Chem.* **2009**, *19*, 6977; d) P. Xu, J. Liu, P. Yan, C. Miao, K. Ye, K. Cheng, J. Yin, D. Cao, K. Li, G. Wang, *J. Mater. Chem. A* **2016**, *4*, 4920; e) L. Qian, X. Tian, L. Yang, J. Mao, H. Yuan, D. Xiao, *RSC Adv.* **2013**, *3*, 1703.
- [30] a) I. Horcas, R. Fernández, J. M. Gómez-Rodríguez, J. Colchero, J. Gómez-Herrero, A. M. Baro, *Rev. Sci. Instrum.* **2007**, *78*, 013705; b) A. Gimeno, P. Ares, I. Horcas, A. Gil, J. M. Gómez-Rodríguez, J. Colchero, J. Gómez-Herrero, *Bioinformatics* **2015**, *31*, 2918.
- [31] a) Z.-S. Wu, A. Winter, L. Chen, Y. Sun, A. Turchanin, X. Feng, K. Müllen, *Adv. Mater.* **2012**, *24*, 5130; b) B. Mendoza-Sánchez, B. Rasche, V. Nicolosi, P. S. Grant, *Carbon* **2013**, *52*, 337; c) J. Lin, C. Zhang, Z. Yan, Y. Zhu, Z. Peng, R. H. Hauge, D. Natelson, J. M. Tour, *Nano Lett.* **2013**, *13*, 72; d) B. S. Singu, K. R. Yoon, *Electrochim. Acta* **2017**, *231*, 749; e) Y. Zou, I. A. Kinloch, R. A. W. Dryfe, *J. Mater. Chem. A* **2014**, *2*, 19495; f) S. Li, C. Yu, J. Yang, C. Zhao, X. Fan, H. Huang, X. Han, J. Wang, X. He, J. Qiu, *ChemElectroChem* **2017**, *4*, 369; g) L. Deng, J. Wang, G. Zhu, L. Kang, Z. Hao, Z. Lei, Z. Yang, Z.-H. Liu, *J. Power Sources* **2014**, *248*, 407; h) Z. Li, L. Wu, L. Wang, A. Gu, Q. Zhou, *Electrochim. Acta* **2017**, *231*, 617; i) M. R. Lukatskaya, O. Mashtalir, C. E. Ren, Y. Dall'Agnese, P. Rozier, P. L. Taberna, M. Naguib, P. Simon, M. W. Barsoum, Y. Gogotsi, *Science* **2013**, *341*, 1502.
- [32] P. Nemes-Incze, Z. Osváth, K. Kamarás, L. P. Biró, *Carbon* **2008**, *46*, 1435.
- [33] E. P. Randviir, D. A. C. Brownson, J. P. Metters, R. O. Kadara, C. E. Banks, *Phys. Chem. Chem. Phys.* **2014**, *16*, 4598.